Research Square

Preprints are preliminary reports that have not undergone peer review.
They should not be considered conclusive, used to inform clinical practice,
or referenced by the media as validated information.

Influence of the Geographical Origin on Properties and Chiral Nematic Self-Assembly of Carboxylated Cellulose Nanocrystals from Degreased Cotton

Jian Huang
College of Environment & Safety Engineering, Fuzhou University
Quan Chen
College of Environment & Safety Engineering, Fuzhou University
Siyu Li
College of Environment & Safety Engineering, Fuzhou University
Yifan Liu
College of Environment & Safety Engineering, Fuzhou University
Yuancai Lv
College of Environment & Safety Engineering, Fuzhou University
Xiaoxia Ye
College of Environment & Safety Engineering, Fuzhou University
Liang Song
College of Environment & Safety Engineering, Fuzhou University
Chunxiang Lin
lcx2010@fzu.edu.cn
College of Environment & Safety Engineering, Fuzhou University
Minghua Liu
College of Environment & Safety Engineering, Fuzhou University

Research Article

Keywords: Carboxylated cellulose nanocrystals, Degreased cotton, Organic acid hydrolysis, Chiral nematic self-assembly, Geographical origins

Posted Date: October 29th, 2026

DOI: https://doi.org/10.21203/rs.3.rs-10371219/v1

License: This work is licensed under a Creative Commons Attribution 4.0 International License. Read Full License

Additional Declarations: No competing interests reported.

Abstract

The intrinsic properties of cellulose are influenced by the geographical origin of its raw material, which in turn significantly affect the characteristics of cellulose nanocrystals (CNCs) derived from organic acid hydrolysis and consequently their chiral self-assembly behavior. In this study, carboxylated cellulose nanocrystals (C-CNCs) were prepared from degreased cotton sourced from six different regions in China via oxalic acid hydrolysis. The influence of geographical origin on the physicochemical properties of the resulting C-CNCs and their chiral nematic self-assembly behavior was systematically investigated. The results revealed that variations were observed among the six C-CNC samples in aspect ratio, carboxyl group content, and Zeta potential. Samples with higher aspect ratios and more negative zeta potentials could develop well-defined chiral nematic liquid crystalline fingerprint textures. And the second critical concentration (C_2) for complete anisotropy decreased with the increasing aspect ratio, while the helical pitch at C_2 increased with both aspect ratio and carboxyl content. Alkaline pretreatment was adopted to pretreat the samples that failed to form chiral nematic phases, aiming to enhance I_β content, crystallinity, and hydroxy-group accessibility by disrupting the hydrogen-bonding network. The resulting N-CNCs exhibited smaller dimensions, higher aspect ratios, and more negative zeta potentials, successfully self-assembling into chiral nematic phases with fingerprint textures and iridescent films.

1. Introduction

Cellulose nanocrystals (CNCs) are nanoscale materials derived from natural cellulose (Peng et al. 2024). Compared with natural cellulose, CNCs possess the characteristics of high aspect ratio, high specific strength, and high surface activity, thus exhibiting extraordinary physical and chemical properties (Venkatesan et al. 2024). One of their most intriguing properties is the ability to self-assemble via evaporation-induced processes into chiral nematic (cholesteric) liquid crystalline phases with a helical architecture. This organization gives rise to unique optical characteristics, such as circular polarization, structural color and photoluminescence, making it promising for applications in chiral catalysis, optical anti-counterfeiting, sensing, and photonic devices (Xing et al. 2023; Feng et al. 2023; Giasson et al. 1988; Gray 2016).

The self-assembly of CNCs into chiral nematic structures was first reported via sulfuric acid hydrolysis (Revol et al. 1992), which established a model system for investigating colloidal self-assembly. However, the formation and characteristics of this liquid crystalline phase are highly sensitive to the surface chemistry and morphological dimensions (e.g., length and diameter) of CNCs, which are in turn dependent on the isolation method and cellulose source (Mahmud et al. 2019). For instance, CNCs produced via sulfuric acid hydrolysis readily form ordered phases, whereas those prepared with hydrochloric acid typically do not (Zhang et al. 2023).

Recently, several alternative methods have been developed as greener routes for CNC isolation, including TEMPO-oxidation (Fan et al. 2022; Geng et al. 2017; He et al. 2017), potassium permanganate oxidation (Zhou et al. 2018), persulfate oxidation (Errezma et al. 2018; Marwanto et al. 2021), and organic acid hydrolysis (Lin et al. 2023; Fu et al. 2020; Li et al. 2017). The latter is particularly attractive due to the milder corrosivity and potential for acid recovery. Studies have shown that dicarboxylic acids can yield carboxylated CNCs that effectively form chiral nematic phases (Fu et al. 2024). Nevertheless, the relatively mild action of organic acids may result in a stronger dependence on the native structure of the cellulose feedstock. Some inherent parameters, such as crystallinity, the I_α/I_β allomorph ratio, and the initial microfibril orientation, vary significantly with the source of the cellulose (Huang et al. 2022), thus affecting the physicochemical properties of the resulting CNCs. For instance, CNCs derived from cotton generally exhibit higher crystallinity and larger aspect ratios compared to those from wood or agricultural residues, which is attributed to the highly ordered native structure of cotton fibers (Hsieh 2013). Even within the same category of cellulose sources, such as cotton, variations in growing conditions, climate, and soil composition can lead to differences in fiber maturity, microfibril angle, and crystallinity (Darawsheh et al. 2022). These subtle but significant differences in the native cellulose structure are subsequently reflected in the properties of the isolated CNCs, including their length, diameter, surface charge density, and thermal stability (Athokpam et al. 2017). Despite the well-documented influence of cellulose source on CNC properties, systematic investigations linking source variability to chiral nematic self-assembly behavior remain scarce. Most studies have focused on CNCs derived from a single source or have compared broadly different sources (e.g., wood vs. cotton) without controlling for other variables (Elazzouzi-Hafraoui et al. 2009; Korolovych et al. 2018; Sacui et al. 2014). This knowledge gap is particularly pertinent for CNCs prepared via organic acid hydrolysis, a green isolation route that has gained increasing attention (Bian et al. 2017; Wang et al. 2017; Lin et al. 2021). Unlike sulfuric acid hydrolysis, which introduces strongly ionizable sulfate ester groups that promote electrostatic stabilization and chiral nematic ordering (Gray 2018; Li et al. 2019; Jordan et al. 2019), organic acid hydrolysis yields carboxylated CNCs with relatively milder surface charges (Parton et al. 2022; Lin et al. 2023; Bian et al. 2017). The self-assembly of such carboxylated CNCs is therefore more susceptible to variations in the intrinsic properties of the cellulose feedstock, as the weaker electrostatic repulsion provides less buffering against differences in particle morphology (Bian et al. 2017). These variations will substantially influence characteristics of the isolated CNCs, especially their aspect ratio (length-to-diameter ratio) or surface chemistry, which are the parameters that affect the phase formation and stability of the liquid crystal (Gao et al. 2022). Despite its fundamental importance, the systematic influence of the cellulose source on the self-assembly of CNCs, particularly those prepared by organic acid hydrolysis, remains largely unexplored.

Herein, the impact of the geographic origin of degreased cotton on the chiral self-assembly of C-CNCs prepared via organic acid hydrolysis was investigated. The properties of degreased cotton from different geographic origins were first characterized, and then the properties of the resulting CNCs were also systematically investigated.

By establishing correlations between the properties of the raw material with the self-assembly behavior and optical characteristics of the resulting C-CNCs, this study aims to identify the dominant factors within the cellulose source that govern the chiral nematic ordering. Our findings are expected to provide theoretical support for the standardized large-scale production and application of organically-acid-hydrolyzed CNCs with predictable photonic properties.

2. Materials and methods

2.1 Materials

Degreased cotton samples sourced from different geographic origins (Yanggu Jingyanggang Sanitary Material Factory, Xuzhou Cotton Field Sanitary Material Co. Ltd, Qingdao Hai's Hainuo Co. Ltd, Fujian Lianjiang Sanitary Material Factory, Hubei Xianning Weijian Medical Co. Ltd, and Shaoxing Sanitary Material Co. Ltd) were pulverized to a particle size of 20–50 μm and air-dried prior to use. Oxalic acid (OA, AR grade) was purchased from Sinopharm. Sodium chloride (NaCl, AR grade), sodium hydroxide (NaOH, AR grade), and polyethylene glycol (PEG 20,000, AR grade) were obtained from Aladdin (China). A dialysis bag (molecular weight cutoff: 8-14 kDa) was procured from Viskase (USA). Ultrapure water was used in all experiments.

2.2 Preparation of C-CNCs suspension and film by organic acid hydrolysis

C-CNCs were isolated from degreased cotton using oxalic acid hydrolysis according to a previously reported method with modifications (Lin et al. 2023). Typically, a mixture of 3 g degreased cotton and 100 g of 80 wt% aqueous oxalic acid solution was heated at 105 °C in an oil bath for 3 h under continuous stirring. After the reaction, approximately 150 mL of warm water was added to quench the process. The mixture was immediately filtered to separate the solid product from the unreacted acid solution. The collected solids were subsequently washed with large amounts of ultrapure water and subjected to repeated centrifugation cycles. The supernatant from the initial centrifugation steps was discarded. Centrifugation was continued until the supernatant appeared turbid, which indicated the presence of colloidal C-CNCs. This turbid supernatant was collected and passed through a high-pressure homogenizer at 800 bar for 3 minutes to obtain a translucent, faint blue suspension.

The resulting suspension was transferred to a dialysis bag (MWCO: 8-14 kDa) and dialyzed against frequent changes of ultrapure water until the conductivity of the external water reached approximately 1 μS/cm. To concentrate the suspension, the dialysis bag was then immersed in an aqueous solution of 10 wt% polyethylene glycol (PEG 20,000) until the C-CNCs concentration reached about 2 wt%. Finally, the concentrated suspension was dialyzed again against ultrapure water until the external water conductivity fell below 1 μS/cm. The yield of C-CNCs was calculated as the mass ratio of the freeze-dried C-CNCs to the initial mass of degreased cotton.

C-CNCs films were prepared using a solution casting method. Briefly, 10 mL of the 2 wt% C-CNCs suspension was sonicated for 5 min using an ultrasonic processor (KQ5200DE, Ultrasonic Equipment Co., Ltd., Shanghai, China). The sonicated suspension was then poured into a plastic Petri dish (35 mm in diameter) and left to evaporate slowly under ambient conditions until a solid film was formed.

For comparison, selected cotton samples (XZ-C, SX-C, and QD-C) were pretreated with 7 wt% NaOH prior to oxalic acid hydrolysis. The corresponding pretreated cotton samples and derived nanocrystals were denoted as XZ-N-C, SX-N-C, and QD-N-C, and XZ-N-CNCs, SX-N-CNCs, and QD-N-CNCs, respectively.

2.3 Characterization

The chemical structures of the samples were characterized by Fourier transform infrared (FTIR) spectroscopy (Nicolet iS5, USA) over a wavenumber range of 500-4000 cm^{-1}. Crystal structures were analyzed by X-ray diffraction (XRD) on a Rigaku MiniFlex 600 diffractometer (Tokyo, Japan) using Cu Kα radiation (λ = 0.154 nm). Surface elemental compositions were determined by X-ray photoelectron spectroscopy (XPS, ESCALAB 250, Thermo Fisher Scientific). Solid-state cross-polarization magic angle spinning ^{13}C nuclear magnetic resonance (CP/MAS ^{13}C NMR) spectra were recorded on an AVANCE III 500 spectrometer (Bruker, Switzerland).

The morphology of C-CNCs was examined by atomic force microscopy (AFM, 5500, Agilent Technologies, USA) operated in tapping mode. The surface carboxyl content was quantified by conductometric titration (916 Ti-Touch, Metrohm, Switzerland), and the zeta potential of the C-CNCs suspensions was measured using a Nano Brook Omni analyzer (Bruker, USA). Optical properties of the suspensions and solid films

were observed under a polarized optical microscope (ZYP-1000E POM, Zhongnuo, China), with macroscopic images captured using a smartphone camera.

3. Results and discussion

3.1 Structural Characteristics of Degreased Cotton from Different Geographic Origins

The inherent structural differences in cellulose raw materials (determined by their geographical origin and growth conditions) might lead to different characteristics of the resulting CNCs, even when subjected to identical preparation processes. To systematically investigate such influence, degreased cotton from six different producing areas (denoted as AB-C, where AB represents the city initials and C for cotton; see Table 1) was selected, and the main physical and chemical properties of the cotton samples were characterized.

The chemical identity of all degreased cotton samples was first confirmed by FTIR spectroscopy (Fig. 1a). All samples exhibited nearly identical spectra, showing characteristic absorption bands for cellulose (Guo and Altaner 2018; Athokpam et al. 2017). A broad and strong band around 3335 cm^{-1} was observed for all samples, corresponding to O-H stretching vibrations, which indicated the presence of an extensive inter-molecular and intra-molecular hydrogen-bonding network. However, notable differences were identified in the O-H bending vibration region (1640-1660 cm^{-1}), which was primarily assigned to the H-O-H bending vibration of adsorbed water. JYG-C, LJ-C, and XN-C showed a band near 1641 cm^{-1}, whereas XZ-C, SX-C, and QD-C displayed a band around 1654 cm^{-1} (Table 1). This slight shift implied the variations in the local hydroxyl environment, which might be attributed to the differences in adsorbed water content, crystallinity, or the proportion of amorphous regions (Guo and Altaner 2018). In particular, the lower wavenumber (1641 cm^{-1}) was often associated with stronger hydrogen-bonded water networks, within a more ordered crystalline structure, while the higher wavenumber (1654 cm^{-1}) suggested the presence of more loosely bound water or a less ordered hydrogen-bonding network (Velazquez et al. 2003; Herrera-Gomez et al. 2001; Chuntonov et al. 2014; Cichosz and Masek 2020).

Table 1 Physical characteristics of degreased cotton samples

cellulose sample	-OH stretching vibration peaks (cm^{-1})	-OH bending vibration peak (cm^{-1})	CrI(%)*	crystal content (%)			I_α/I_β
				I_α	I_β	para-Crystalline	
JYG-C	3334.2	1641.5	73.14	17.28	60.38	22.34	0.29
LJ-C	3334.9	1640.6	78.96	21.12	64.73	14.15	0.33
XN-C	3333.5	1640.9	73.79	20.04	61.89	18.07	0.32
XZ-C	3334.1	1654.1	65.90	29.25	55.21	15.54	0.53
SX-C	3335.4	1654.0	63.06	23.46	45.13	31.41	0.52
QD-C	3334.2	1654.1	64.65	28.92	54.21	17.04	0.54

Differences in the supramolecular architecture of cellulose from different geographical origins were further investigated by XRD analysis. The data presented in Fig. 1b confirmed the typical cellulose I structure for all samples, with characteristic peaks at 2θ = 15°, 22.5°, and 34°. However, the crystallinity index (CrI), calculated using the Segal method with baseline subtraction (Segal. et al. 1959; Kirui et al. 2019) revealed significant differences. The CrI values for JYG-C, LJ-C and XN-C were notably higher than those for XZ-C, QD-C, and SX-C (Fig. 1b, Table 1). This variation in CrI was likely attributable to differences in growth environments, such as soil composition and climate, which influence the order within the cellulose crystalline regions (Manju et al. 2023).

Further insights into the crystalline structure were obtained through solid-state CP/MAS ^{13}C NMR. The spectra presented in Fig. 1c showed that the regions at 100-110 ppm was assigned to the C1 carbon in ordered cellulose structures, and and the region at 80–91 ppm was assigned to the C4 carbon signals of cellulose, including crystalline and disordered contributions (Park et al. 2009). It was found that natural cellulose mainly consists of cellulose I_α and I_β with variable proportions. The I_α form is typically associated with a triclinic unit cell, while the I_β form is characterized by a monoclinic unit cell (Szymańska-Chargot et al. 2011; Peter 2021). Quantification of the cellulose I_α and I_β allomorphs could be estimated by spectral deconvolution of C-1 peak for cellulose I_α (105.2 ppm), I_β (103.7 and 105.6 ppm) and para-crystalline (104.5 ppm) (Fig. 1d) (Villares et al. 2017; Xiaolan et al. 2018). The relative ratio of I_α to I_β was calculated as the area ratio of the peak at 105.2 ppm to the sum of the peaks at 103.7 ppm and 105.6 ppm. As presented in Table 1, the relative amount of cellulose I_β in JYG-C, XN-C, and LJ-C was higher than that in others due to the lower I_α/I_β values, indicating higher crystallinity index of these

samples (Szymańska-Chargot et al. 2011). The results were in good agreement with the XRD data, providing a more detailed understanding of the crystalline differences.

XPS analysis provided insights into the surface chemical composition of the cotton samples(Fig. 1e). The survey spectra of all samples exhibited highly identical. However, obvious differences were observed in the high-resolution of C 1s spectra, which could be deconvoluted into three components: C1 (284.6 eV, attributed to C-C/C-H bonds from saturated carbon skeletons or trace adsorbed hydrocarbons), C2 (286.5 eV, assigned to C-O bonds derived from hydroxyl groups (-OH) and glycosidic linkages (C-O-C) in cellulose), and C3 (288.0 eV, corresponds to C=O or O-C-O bonds from trace oxidized moieties or impurities) (Vizireanu et al. 2018). Fig. 1f showed that samples of JYG-C, LJ-C, XZ-C, and QD-C exhibited a higher proportion of the C2 component (C-O bond) . As established, a relatively higher C2 proportion indicated a surface that is predominantly composed of cellulosic material with abundant hydroxyl groups, implying superior surface hydrophilicity and chemical accessibility for subsequent reactions (Park et al. 2010; Eyley and Thielemans 2014).

High-resolution of O 1s spectra were deconvoluted into two components, C-OH (532.0 eV, representing free hydroxyl groups) and C-OH...O (531.0 eV, representing hydrogen-bonded hydroxyls) (Vera et al. 2023). Results presented in Fig. 1g demonstrated that JYG-C, XN-C and LJ-C showed a higher content of free hydroxyl groups (C-OH), while XZ-C, SX-C, and QD-C exhibited a significantly higher proportion of hydrogen-bonded hydroxyls (C-OH...O). A higher content of free hydroxyl groups meant a lower density of the hydrogen-bonding network, which might promote the penetration of hydrated hydrogen ions during acid hydrolysis, thus leading to higher CNCs yields (Dagnino et al. 2025).

In summary, the comprehensive characterization demonstrated that although the degreased cotton samples from different producing areas were chemically identical, they differed in several supramolecular structural parameters, including crystallinity, the relative cellulose I_{β} content, surface hydroxyl accessibility, and hydrogen-bonding environment. These source-dependent features were expected to affect the hydrolysis efficiency, as well as the properties of the resulting C-CNCs.

3.2 Properties of the resulting C-CNCs

Cotton samples from different geographical origins were subjected to identical organic acid hydrolysis conditions to yield C-CNCs, as detailed in Section 2.2. For clarity, the resulting nanocrystals were denoted as AB-CNCs, where “AB” corresponded to the city initials of the original cotton samples. As summarized in Table 2, the yield of C-CNCs varied considerably, ranging from approximately 5% to over 21% under the same hydrolysis condition. This significant variation could be attributed to inherent structural differences among the raw materials. Specifically, samples of JYG-C, LJ-C, and XN-C, which exhibited higher yields, were characterized by weaker hydrogen-bonding networks and a greater content of free hydroxyl groups (Miao et al. 2022; Chen et al. 2016b). This structural profile likely facilitated more efficient cleavage of glycosidic bonds during hydrolysis, thereby enhancing the conversion efficiency to nanocrystals.

Table 2 Characteristics of C-CNCs Samples

Cellulose sample	Yield (%)	Length range (nm)	Average length (nm)	Width range (nm)	Average width (nm)	Aspect ratio	Carboxyl content (mmol/g)	Surface charge (mV)	CrI (%)	C_1	C_2	Pitch (μm)
JYG-CNCs	21.84%	316~953	560±133	20~136	79±27	7.1	0.123	-33.650	82.95	0.78	2.86	14.3
LJ-CNCs	17.20%	257~854	546±114	20~131	72±27	7.6	0.101	-35.440	81.68	0.69	2.79	12.1
XN-CNCs	18.17%	261~992	529±175	20~178	80±33	6.6	0.101	-41.405	85.53	0.85	2.92	11.1
XZ-CNCs	7.57%	392~878	604±107	58~186	105±27	5.8	0.083	-28.710	78.03	N.D.	N.D.	N.D.
SX-CNCs	5.63%	427~1012	722±125	60~171	117±26	6.2	0.093	-20.245	72.05	N.D.	N.D.	N.D.
QD-CNCs	13.21%	305~904	608±126	22~271	114±52	5.3	0.078	-27.825	73.77	N.D.	N.D.	N.D.

The morphological characteristics of the C-CNCs were analyzed by AFM, as shown in Fig. 2a-f. The images revealed polydisperse, needle-shaped nanocrystals. Quantitative analysis of the particle dimensions (Fig. S1 and Table 2) showed that the width ranged from 70 to 110 nm and the length from 250 to 1000 nm, yielding aspect ratios between 5.3 and 7.6. Notably, C-CNCs derived from JYG, LJ and XN cotton samples generally exhibited higher aspect ratios, along with smaller widths and shorter lengths, compared to those from XZ, SX, and QD samples. Such variations in morphological was likely attributed to the stronger hydrogen bonding within the original cellulose fibers of the latter group, which could impart greater resistance to acid hydrolysis, thereby resulting in larger, less elongated nanocrystals with lower aspect ratios (Lin et al. 2023).

XRD patterns of all C-CNCs samples (Fig. 2g) confirmed the characteristic crystalline structure of cellulose I (Wang et al. 2019). The values of CrI, summarized in Table 2, indicated a clear increase in crystallinity for all C-CNCs compared with their corresponding original degreased cotton. This enhancement was attributed to the selective hydrolysis and removal of amorphous region during oxalic acid treatment (Lin et al. 2023). Notably, JYG-CNCs, LJ-CNCs, and XN-CNCs exhibited higher CrI values than XZ-CNCs, QD-CNCs, and SX-CNCs. The reason might be ascribed to the higher initial proportion of cellulose I_β allomorph in these samples (Xiang et al. 2003; Lin et al. 2023).

The chemical structures of the C-CNCs samples were analyzed by FTIR spectroscopy (Fig. 2h). Compared with the original degreased cotton, all C-CNCs spectra exhibited a new peak at 1728 cm^{-1}, corresponding to C=O stretching vibrations, confirming the introduction of surface carboxyl groups via esterification during hydrolysis (Jia and Liu 2019). The carboxyl group content and surface charge of each C-CNCs sample were further quantified (Table 2). The carboxyl content ranged from 0.078 to 0.123 mmol/g, and the zeta potential varied between -20 and -41 mV. JYG-CNCs, LJ-CNCs, and XN-CNCs presented higher carboxyl content and surface charge than XZ-CNCs, QD-CNCs, and SX-CNCs. The variations were associated with the proportion of free hydroxyl groups in the cellulose raw materials (Fig. 1g), a higher content of free hydroxyl groups promoted esterification, leading to greater carboxylation on the resulting C-CNCs surfaces (Seta et al. 2020).

Based on the above analyses, it can be concluded that C-CNCs derived from cotton of different geographical origins exhibited significant variations in yield, morphology, crystallinity, and surface chemistry under identical organic acid hydrolysis conditions. The differences were primarily governed by the inherent supramolecular architecture of the raw cellulose. Specifically, cotton samples from JYG, LJ, and XN, characterized by weaker hydrogen-bonding networks, a higher content of free hydroxyl groups, and a greater proportion of the cellulose I_β allomorph, displayed enhanced reactivity during hydrolysis, thus leading to C-CNCs with higher yields, larger aspect ratios, elevated crystallinity indices, and richer surface carboxylation. In contrast, cellulose from XZ, SX, and QD, possessing stronger inter- and intra-molecular hydrogen bonds and a more compact structure, offered greater resistance to acid erosion, resulting in nanocrystals with larger dimensions, lower aspect ratios, and comparatively reduced crystallinity and surface functionalization.

3.3 Chiral Self-Assembly Behavior of C-CNCs

The chiral characteristics of C-CNCs are significantly influenced by their properties, such as aspect ratio, surface charge, and functional groups (Elazzouzi-Hafraoui et al. 2009). As indicated previously, C-CNCs isolated from degreased cotton originating from different geographical regions exhibited distinct intrinsic properties, suggesting potential variations in their self-assembly behavior. To investigate the chiral nature of these C-CNCs, the chiral self-assembly behavior was examined. POM images of suspensions for all C-CNCs samples were presented in Fig. 3a. Characteristic fingerprint textures, indicative of a chiral nematic liquid crystal phase, were observed only for the samples of JYG-CNCs, LJ-CNCs, and XN-CNCs. No fingerprint texture was observed in XZ-CNCs, QD-CNCs and SX-CNCs, which was likely attributed to the lower aspect ratios and surface charges of samples (Elazzouzi-Hafraoui et al. 2009). A lower aspect ratio made the particles more prone to forming random aggregates or isotropic phases, rather than assembling into helical arrangements (Raghuwanshi et al. 2023). Simultaneously, the lower carboxyl group content and surface charge facilitated particle aggregation, leading to the formation of a gel state instead of an ordered liquid crystalline phase (Jia and Liu 2019).

To further investigate the self-assembly behavior of C-CNCs, the formation process of the chiral nematic liquid crystal phase was monitored for three samples: JYG-CNCs, LJ-CNCs, and XN-CNCs. Fig. 3b presented the POM images of JYG-CNCs suspensions at different concentrations. It could be seen that the suspension appeared optically isotropic at 0.3 wt%, showing no color variation under crossed polarizers. When the concentration reached 1.0 wt%, birefringence and tactoids became visible. Further increases in concentration enhanced birefringence, eventually leading to phase separation and the emergence of fingerprint textures. At 3.1 wt%, a well-defined fingerprint texture was observed, indicating a fully anisotropic suspension. Similar self-assembly progression was noted for LJ-CNCs and XN-CNCs, as shown in Fig. 3c-d.

In these fingerprint patterns, the distance between adjacent stripes corresponds to a 180° rotation of the chiral nematic structure, equivalent to half of the helical pitch (P) (Song et al. 2024). As illustrated in Fig. 3b-d, the pitch decreased with increasing concentration. This trend could be explained by the closer packing of rod-like C-CNCs particles at higher concentrations, which gradually compressed the helical structure (Frka-Petesic et al. 2019). Ultimately, the fingerprint textures fixed within the film at a specific pitch, yielding macroscopic structural color iridescence (Qu et al. 2022). C-CNCs derived from degreased cotton of different regional origins, despite undergoing identical hydrolysis treatments, exhibited distinct self-assembly behaviors, reflected in variations in the second critical concentration (C_2) and helical pitch (Lin et al. 2021). Here, C_2 denotes the concentration at which it becomes fully anisotropic. As listed in Table 2, the C_2 values for JYG-CNCs, LJ-CNCs, and XN-CNCs were 2.86 wt%, 2.79 wt%, and 2.92 wt%, with corresponding aspect ratios of 7.1, 7.6, and 6.6, respectively. The sample with the highest aspect ratio (LJ-CNCs) showed the lowest C_2, supporting the trend that a larger aspect ratio promotes anisotropic ordering and self-assembly into chiral arrangements at lower particle densities (Qu et al. 2022). The digital

photographs of the corresponding films further revealed that only the C-CNCs capable of forming chiral nematic phases in suspension produced iridescent structural-color films, whereas the non-assembled samples yielded optically disordered films without obvious color reflection (Fig. 4). Additionally, the cross-sectional SEM images of the JYG-CNCs, LJ-CNCs and XN-CNCs films (Fig. 4) revealed highly ordered periodic layered structure, which was the characteristic of the chiral nematic organization. These observations provided complementary evidence that corroborates the chiral nematic order identified by POM analysis.

Furthermore, the helical pitch of the chiral nematic phase at C_2 was also measured (Table 2), and JYG-CNCs showed the highest value of 14.3 μm. The reason might be ascribed to the higher carboxyl content and surface charge, which would strengthen the interparticle electrostatic repulsion and contributed to its larger pitch (Browne et al. 2023; Zhang et al. 2018; Jiang et al. 2021).

3.4 Alkali Pretreatment for Controlled Chiral Assembly of CNCs

As discussed above, the failure to form ordered chiral nematic phases for samples of XZ-CNCs, QD-CNCs and SX-CNCs was primarily ascribed to the lower aspect ratios and surface charges caused by the stronger hydrogen bonding within the cellulose crystals. Alkaline treatment is considered to be an efficient way for weakening the hydrogen bonding network (Nan et al. 2017). Herein, 7 wt% NaOH solution was employed to pretreat the degreased cotton before acid hydrolysis, aiming to disrupt its internal hydrogen-bonding network. The pretreated degreased cotton samples were labeled as AB-N-C, and the resulting CNCs were labeled as AB-N-CNCs.

To evaluate the impact of alkaline pretreatment, the structural changes in the cotton after alkali treatment were characterized. Fig. 5a presented the XRD patterns and CrI of the three samples of XZ-N-C, SX-N-C, and QD-N-C. All samples displayed characteristic diffraction peaks of cellulose I. Notably, the CrI values were higher than those of the corresponding untreated samples (XZ-C, SX-C, and QD-C), which could be attributed to the interaction between cellulose and Na^+ ions during alkaline treatment. The small ionic radius of Na^+ allowed it to penetrate rapidly into the amorphous regions of cellulose, promoting a conformational rearrangement toward a more ordered and stable structure (Nan et al. 2017).

Table 3 Positions of -OH groups in AB-N-C FTIR and crystallinity content

cellulose samples	-OH stretching vibration peak (cm^{-1})	-OH bending vibration peak (cm^{-1})	CrI* (%)	crystal content (%)			I_α/I_β
				I_α	I_β	para-Crystalline	
XZ-N-C	3335.2	1642.2	76.03	18.18	57.66	24.16	0.32
SX-N-C	3334.9	1641.4	77.12	14.28	65.25	20.47	0.22
QD-N-C	3334.8	1644.9	75.33	22.29	60.01	17.70	0.37

The solid-state ^{13}C CP/MAS NMR spectra of the AB-N-C samples were shown in Fig. 5b. The chemical shift ranges were found to be consistent with those before pretreatment, indicating that the chemical structure of cellulose did not change during pretreatment. To gain further insight, the C1 signal was fitted using a Lorentzian model. It could be seen that the proportion of cellulose I_β increased to 57.66%, 65.25%, and 60.01% for XZ-N-C, SX-N-C, and QD-N-C, respectively, accompanied by a corresponding decrease in cellulose I_α. The increased relative contribution of cellulose I_β indicated a change in the crystalline organization toward a more I_β-rich cellulose I structure (Fig. S2 and Table 3). FTIR analysis was used to further examine the chemical structures (Fig. 5c and Table 3). Results demonstrated that after alkaline pretreatment, the O-H bending vibration peak of degreased cotton exhibited a red-shift, indicating a reduction in the strength of intermolecular hydrogen bonds (Grech et al. 1978).

XPS results revealed changes in surface chemical composition after pretreatment. As illustrated in Fig. S3 and Fig. 5d, the O 1s spectra of QD-N-C, SX-N-C, and XZ-N-C showed a higher proportion of C-OH groups compared to their untreated counterparts. The increase was attributed to the disruption of hydrogen bonds (e.g., C-OH...O) and exposes more free hydroxyl groups due to the penetration of Na^+ ions into amorphous domains (Chen et al. 2016a). The increased number of free -OH groups facilitated the hydrolysis and esterification of cellulose, thereby improving the characteristics of C-CNCs.

The resulting C-CNCs from pretreated degreased cotton were also subjected to physical and chemical characterization. XRD patterns of QD-N-CNCs, SX-N-CNCs, and XZ-N-CNCs (Fig. 5e) confirmed retention of the cellulose I structure with higher CrI values than their untreated counterparts, reflecting enhanced crystalline order from NaOH pretreatment (Chirayil et al. 2014; Kugo et al. 2024). FTIR spectra (Fig. 5f) showed a distinct 1728 cm^{-1} band, indicating successful surface carboxylation, consistent with improved hydroxyl accessibility and esterification efficiency after alkaline pretreatment (Jia and Liu 2019; Seta et al. 2020). The yields of C-CNCs were determined and are presented in Table 4. The data showed that the yields for XZ-N-CNCs, SX-N-CNCs, and QD-N-CNCs reached 23.76%, 18.37%, and 25.62%,

respectively, which were higher than those of the corresponding untreated samples (Fig. 5g). This increase indicated that alkaline pretreatment improved hydrolysis efficiency by enhancing hydroxyl accessibility and reducing the resistance imposed by the original hydrogen-bonding network (Bali et al. 2015). AFM images (Fig. S4a-c) and the data presented in Table 4 further showed that AB-N-CNCs possessed smaller dimensions and larger aspect ratios than the untreated samples. In addition, the surface carboxyl content, zeta potential, and CrI of AB-N-CNCs were also improved (Fig. 5h-i and Table 4). These changes were consistent with the more efficient hydrolysis and more effective surface carboxylation after pretreatment.

Table 4 Characteristics of AB-N-CNCs Samples

cellulose sample	yield (%)	length range (nm)	average length (nm)	Width range (nm)	average width (nm)	aspect ratio	carboxyl content (mmol/g)	surface charge (mV)	CrI (%)	C_1	C_2	pitch (μm)
XZ-N-CNCs	23.76%	322~769	525±92	20~126	81±20	6.5	0.139	-32.890	80.40	0.88	3.07	11.7
SX-N-CNCs	18.37%	279~868	529±121	20~135	81±26	6.6	0.118	-30.375	81.96	0.82	2.89	10.9
QD-N-CNCs	25.62%	252~721	483±113	23~153	75±26	6.4	0.124	-34.235	82.85	0.90	3.13	10.5

As described above, the AB-N-CNCs exhibited smaller dimensions, higher aspect ratios, and greater surface charge, all of which were favorable for the formation of chiral nematic liquid crystals (Jiang et al. 2021). Therefore, the self-assembly behavior of XZ-N-CNCs, SX-N-CNCs, and QD-N-CNCs was investigated. Fig. 6a presented the POM images of the three samples, it could be seen that fingerprint textures were observed when the concentrations of XZ-N-CNCs, SX-N-CNCs, and QD-N-CNCs suspensions reached 3.1 wt%, 3.3 wt%, and 2.9 wt%, respectively, confirming the formation of chiral nematic phases. The digital photographs of the corresponding AB-N-CNCs films further supported the recovery of chiral self-assembly after alkaline pretreatment. As shown in Fig. 6b, XZ-N-CNCs, SX-N-CNCs, and QD-N-CNCs all formed films with visible iridescent structural colors, in sharp contrast to the dull and non-iridescent films obtained from the untreated samples. SEM images of cross-sections of these films (Fig. 6b) also confirmed their chiral characteristics.

The self-assembly behavior of the three samples at varying concentrations was systematically observed by POM, as shown in Fig. S5. The results revealed that the chiral nematic self-assembly process of N-CNCs suspensions was analogous to that of C-CNCs suspensions. The self-assembly characteristics of AB-N-CNCs were summarized in Table 4, in which the C_2 values of the AB-N-CNCs could be determined after pretreatment and were slightly higher than those of the naturally assembling JYG-CNCs, LJ-CNCs, and XN-CNCs. These variations in C_2 and pitch for N-CNCs were primarily attributable to their relatively lower aspect ratios. A lower aspect ratio elevated the concentration required for the suspension to become fully anisotropic and simultaneously led to a more tightly packed helical arrangement.

Conclusions

This study demonstrated that the properties and self-assembly behavior of C-CNCs were significantly influenced by the source of the cellulose feedstock. Degreased cotton from different producing areas exhibited variations in physical characteristics, notably in the proportion of cellulose I_β and the content of free hydroxy groups. These inherent properties directly governed the performance of the resulting C-CNCs. Cellulose with a higher cellulose I_β content and more free hydroxy groups yielded C-CNCs possessing larger aspect ratios and more negative zeta potentials, which in turn facilitated the formation of chiral nematic liquid crystalline phases at a lower second critical concentration (C_2) and with a larger helical pitch. Furthermore, alkaline pretreatment could effectively weaken the hydrogen-bonding network of cellulose, and modulate the physical structure of cellulose by increasing the cellulose Iβ fraction and free hydroxy-group content. These structural changes increased the aspect ratio and resulted in more negative zeta potentials of the resulting C-CNCs, thereby promoting their spontaneous assembly into well-ordered chiral nematic phases.

Statements & Declarations

Acknowledgements

This work was sponsored by the Central Government Guides Local Science and Technology Development Projects (2024L3001).

Competing Interests

The authors declare that they have no known competing financial interests or personal relationships that could have appeared to influence the work reported in this paper.

Funding

This work was supported by the Central Government Guides Local Science and Technology Development Projects (2024L3001).

Data Availability Statement

Data will be made available on request.

Author Contributions

All authors contributed to the study conception and design. Conceptualization and methodology were performed by Jian Huang and Chunxiang Lin. Material preparation, experimental investigation, and data collection were performed by Jian Huang, Siyu Li, Liang Song, Yuancai Lv, and Xiaoxia Ye. Data curation, validation, formal analysis, and visualization were performed by Quan Chen, Siyu Li, Yifan Liu, Yuancai Lv, and Xiaoxia Ye. The first draft of the manuscript was written by Jian Huang. Quan Chen and Chunxiang Lin contributed to manuscript review and editing. Chunxiang Lin was responsible for project administration and funding acquisition. Minghua Liu contributed to resources and project administration. All authors read and approved the final manuscript.

References

1. Athokpam B, Ramesh S G, Mckenzie R H (2017) Effect of hydrogen bonding on the infrared absorption intensity of OH stretch vibrations. Chemical Physics. 488: 43-54 https://doi.org/10.1016/j.chemphys.2017.03.006
2. Bali G, Meng X Z, Deneff J I, et al (2015) The Effect of Alkaline Pretreatment Methods on Cellulose Structure and Accessibility. Chemsuschem. 8: 275-279 https://doi.org/10.1002/cssc.201402752
3. Bian H, Chen L, Wang R, Zhu J (2017) Green and Low-cost Production of Thermally Stable and Carboxylated Cellulose Nanocrystals and Nanofibrils Using Highly Recyclable Dicarboxylic Acids. J Vis Exp. https://doi.org/10.3791/55079
4. Browne C, Raghuwanshi V S, Garnier G, Batchelor W (2023) Modulating the chiral nematic structure of cellulose nanocrystal suspensions with electrolytes. Journal of Colloid and Interface Science. 650: 1064-1072 https://doi.org/10.1016/j.jcis.2023.07.073
5. Chen J H, Xu J K, Huang P L, Sun R C (2016a) Effect of alkaline pretreatment on the preparation of regenerated lignocellulose fibers from bamboo stem. Cellulose. 23: 2727-2739 https://doi.org/10.1007/s10570-016-0983-1
6. Chen L H, Zhu J Y, Baez C, et al (2016b) Highly thermal-stable and functional cellulose nanocrystals and nanofibrils produced using fully recyclable organic acids. Green Chemistry. 18: 3835-3843 https://doi.org/10.1039/c6gc00687f
7. Chirayil C J, Joy J, Mathew L, et al (2014) Isolation and characterization of cellulose nanofibrils from Helicteres isora plant. Industrial Crops and Products. 59: 27-34 https://doi.org/10.1016/j.indcrop.2014.04.020
8. Chuntonov L, Kumar R, Kuroda D G (2014) Non-linear infrared spectroscopy of the water bending mode: direct experimental evidence of hydration shell reorganization? Phys Chem Chem Phys. 16: 13172-13181 https://doi.org/10.1039/c4cp00643g
9. Cichosz S, Masek A (2020) IR Study on Cellulose with the Varied Moisture Contents: Insight into the Supramolecular Structure. Materials. 13: 4573 https://doi.org/10.3390/ma13204573
10. Dagnino E P, Ehman N, Area M C (2025) Recent Advances in Cellulose Nanocrystal Production from Green Methods. Processes. 13: 790 https://doi.org/10.3390/pr13030790
11. Darawsheh M K, Beslemes D, Kouneli V, et al (2022) Environmental and Regional Effects on Fiber Quality of Cotton Cultivated in Greece. Agronomy. 12: 943 https://doi.org/10.3390/agronomy12040943
12. Elazzouzi-Hafraoui S, Putaux J-L, Heux L (2009) Self-assembling and Chiral Nematic Properties of Organophilic Cellulose Nanocrystals. The Journal of Physical Chemistry B. 113: 11069-11075 https://doi.org/10.1021/jp900122t
13. Errezma M, Ben Mabrouk A, Magnin A, et al (2018) Surfactant-free emulsion Pickering polymerization stabilized by aldehyde-functionalized cellulose nanocrystals. Carbohydrate polymers. 202: 621-630 https://doi.org/10.1016/j.carbpol.2018.09.018
14. Eyley S, Thielemans W (2014) Surface modification of cellulose nanocrystals. Nanoscale. 6: 7764-7779 https://doi.org/10.1039/c4nr01756k
15. Fan W, Li J Q, Wei L H, Xu Y (2022) Carboxylated cellulose nanocrystal films with tunable chiroptical properties. Carbohydrate polymers. 289: 9 https://doi.org/10.1016/j.carbpol.2022.119442

16. Feng K, Wei G D, Liu Y B, et al (2023) Cellulose Nanocrystals Chiral Nematic Coating with Reversible Multiple-Stimuli-Responsive Coloration. ACS Sustainable Chemistry & Engineering. 11: 8374-8385 https://doi.org/10.1021/acssuschemeng.3c01782
17. Frka-Petesic B, Kamita G, Guidetti G, Vignolini S (2019) Angular optical response of cellulose nanocrystal films explained by the distortion of the arrested suspension upon drying. Physical Review Materials. 3: 25 https://doi.org/10.1103/PhysRevMaterials.3.045601
18. Fu Q, Zheng T T, Wan W X, et al (2024) Liquid crystal phase behavior of oxalated cellulose nanocrystal and optical films with controllable structural color induced by centripetal force. International journal of biological macromolecules. 280: 12 https://doi.org/10.1016/j.ijbiomac.2024.135883
19. Fu X, Ji H, Wang B, et al (2020) Preparation of thermally stable and surface-functionalized cellulose nanocrystals by a fully recyclable organic acid and ionic liquid mediated technique under mild conditions. Cellulose. 27: 1289-1299 https://doi.org/10.1007/s10570-019-02875-2
20. Gao M G, Shang Y Z, Li B, Du H S (2022) Sustainable preparation of cellulose nanocrystals: state of the art and perspectives. Green Chemistry. 24: 9346-9372 https://doi.org/10.1039/d2gc03003a
21. Geng L, Peng X, Zhan C, et al (2017) Structure characterization of cellulose nanofiber hydrogel as functions of concentration and ionic strength. Cellulose. 24: 5417-5429 https://doi.org/10.1007/s10570-017-1496-2
22. Giasson J, Revol J F, Ritcey A M, Gray D G (1988) ELECTRON-MICROSCOPIC EVIDENCE FOR CHOLESTERIC STRUCTURE IN FILMS OF CELLULOSE AND CELLULOSE-ACETATE. Biopolymers. 27: 1999-2004 https://doi.org/10.1002/bip.360271210
23. Gray D G (2016) Recent Advances in Chiral Nematic Structure and Iridescent Color of Cellulose Nanocrystal Films. Nanomaterials. 6: 9 https://doi.org/10.3390/nano6110213
24. Gray D G (2018) Order and gelation of cellulose nanocrystal suspensions: an overview of some issues. Philos Trans A Math Phys Eng Sci. 376 https://doi.org/10.1098/rsta.2017.0038
25. Grech E, Malarski Z, Romanowski H, Sobczyk L (1978) Stochastic model of strong hydrogen bonds and the temperature effect on IR spectra. Journal of Molecular Structure. 47: 317-321 https://doi.org/10.1016/0022-2860(78)87197-X
26. Guo F, Altaner C M (2018) Molecular deformation of wood and cellulose studied by near infrared spectroscopy. Carbohydrate polymers. 197: 1-8 https://doi.org/10.1016/j.carbpol.2018.05.064
27. He J, Liu S, Li L, Piao G (2017) Lyotropic liquid crystal behavior of carboxylated cellulose nanocrystals. Carbohydrate polymers. 164: 364-369 https://doi.org/10.1016/j.carbpol.2017.01.080
28. Herrera-Gomez A, Velazquez G, Martin-Polo M (2001) Analysis of the water bound to a polymer matrix by infrared spectroscopy. Journal of Applied Physics. 89: 5431-5437 https://doi.org/10.1063/1.1365427
29. Hsieh Y-L (2013) Cellulose nanocrystals and self-assembled nanostructures from cotton, rice straw and grape skin: a source perspective. Journal of Materials Science. 48: 7837-7846 https://doi.org/10.1007/s10853-013-7512-5
30. Huang C L, Yu H Y, Abdalkarim S Y H, et al (2022) A comprehensive investigation on cellulose nanocrystals with different crystal structures from cotton via an efficient route. Carbohydrate polymers. 276: 10 https://doi.org/10.1016/j.carbpol.2021.118766
31. Jia W, Liu Y (2019) Two characteristic cellulose nanocrystals (CNCs) obtained from oxalic acid and sulfuric acid processing. Cellulose. 26: 8351-8365 https://doi.org/10.1007/s10570-019-02690-9
32. Jiang S, Farooq A, Han F Y, Liu L F (2021) Investigation of a Widely Applicable Process for Extracting Carboxyl-rich Cellulose Nanocrystal (CNC). Fibers and Polymers. 22: 647-657 https://doi.org/10.1007/s12221-021-0279-4
33. Jordan J H, Easson M W, Condon B D (2019) Alkali Hydrolysis of Sulfated Cellulose Nanocrystals: Optimization of Reaction Conditions and Tailored Surface Charge. Nanomaterials (Basel). 9 https://doi.org/10.3390/nano9091232
34. Kirui A, Ling Z, Kang X, et al (2019) Atomic resolution of cotton cellulose structure enabled by dynamic nuclear polarization solid-state NMR. Cellulose. 26: 329-339 https://doi.org/10.1007/s10570-018-2095-6
35. Korolovych V F, Cherpak V, Nepal D, et al (2018) Cellulose nanocrystals with different morphologies and chiral properties. Polymer. 145: 334-347 https://doi.org/10.1016/j.polymer.2018.04.064
36. Kugo Y, Nomura S, Isono T, et al (2024) Elucidating the structural changes of cellulose molecules and dynamics of Na ions during the crystal transition from cellulose I to II in low temperature and low concentration NaOH solution. Carbohydrate polymers. 332: 11 https://doi.org/10.1016/j.carbpol.2024.121907
37. Li C, Evans J, Wang N, et al (2019) pH dependence of the chirality of nematic cellulose nanocrystals. Sci Rep. 9: 11290 https://doi.org/10.1038/s41598-019-47834-w
38. Li D, Henschen J, Ek M (2017) Esterification and hydrolysis of cellulose using oxalic acid dihydrate in a solvent-free reaction suitable for preparation of surface-functionalised cellulose nanocrystals with high yield. Green Chemistry. 19: 5564-5567

https://doi.org/10.1039/C7GC02489D

39. Lin C X, Chen B Q, Liu Y S, et al (2021) Carboxylated cellulose nanocrystals with chiral nematic property from cotton by dicarboxylic acid hydrolysis. Carbohydrate polymers. 264: 10 https://doi.org/10.1016/j.carbpol.2021.118039
40. Lin C X, Wang P, Liu Y F, et al (2023) Chiral Self-Assembly Behavior of Carboxylated Cellulose Nanocrystals Isolated by Recyclable Oxalic Acid from Degreasing Cotton. ACS Sustainable Chemistry & Engineering. 11: 8035-8043 https://doi.org/10.1021/acssuschemeng.3c00118
41. Mahmud M M, Perveen A, Jahan R A, et al (2019) Preparation of different polymorphs of cellulose from different acid hydrolysis medium. International journal of biological macromolecules. 130: 969-976 https://doi.org/10.1016/j.ijbiomac.2019.03.027
42. Manju V V, Ranjini S S, Vadhiyar R, Somashekar R (2023) Application of powder XRD to compute crystallite shape of cotton fibers from different countries. Nuclear and Particle Physics Proceedings. 336-338: 41-44 https://doi.org/10.1016/j.nuclphysbps.2023.07.022
43. Marwanto M, Maulana M I, Febrianto F, et al (2021) Characteristics of nanocellulose crystals from balsa and kapok fibers at different ammonium persulfate concentrations. Wood Science and Technology. 55: 1319-1335 https://doi.org/10.1007/s00226-021-01319-0
44. Miao C W, Mauran D, Hamad W Y (2022) How hydrogen-bonding interactions and nanocrystal aspect ratios influence the morphology and mechanical performance of polymer nanocomposites reinforced with cellulose nanocrystals. Soft Matter. 18: 4572-4581 https://doi.org/10.1039/d2sm00140c
45. Nan F C, Nagarajan S, Chen Y W, et al (2017) Enhanced Toughness and Thermal Stability of Cellulose Nanocrystal Iridescent Films by Alkali Treatment. ACS Sustainable Chemistry & Engineering. 5: 8951-8958 https://doi.org/10.1021/acssuschemeng.7b01749
46. Park S, Johnson D K, Ishizawa C I, et al (2009) Measuring the crystallinity index of cellulose by solid state 13C nuclear magnetic resonance. Cellulose. 16: 641-647 https://doi.org/10.1007/s10570-009-9321-1
47. Park S, Baker J O, Himmel M E, et al (2010) Cellulose crystallinity index: measurement techniques and their impact on interpreting cellulase performance. Biotechnology for Biofuels. 3: 10 https://doi.org/10.1186/1754-6834-3-10
48. Parton T G, Parker R M, Van De Kerkhof G T, et al (2022) Chiral self-assembly of cellulose nanocrystals is driven by crystallite bundles. Nature communications. 13: 2657 https://doi.org/10.1038/s41467-022-30226-6
49. Peng Y Y, Wei X Y, Liang Y, et al (2024) Advances in structural color composite films based on cellulose nanocrystals. Industrial Crops and Products. 221: 18 https://doi.org/10.1016/j.indcrop.2024.119294
50. Peter Z (2021) Order in cellulosics: Historical review of crystal structure research on cellulose. Carbohydrate polymers. 254: 117417 https://doi.org/10.1016/j.carbpol.2020.117417
51. Qu D, Rojas O J, Wei B, Zussman E (2022) Responsive Chiral Photonic Cellulose Nanocrystal Materials. Advanced Optical Materials. 10: 26 https://doi.org/10.1002/adom.202201201
52. Raghuwanshi V S, Browne C, Batchelor W, Garnier G (2023) Self-assembly of cellulose nanocrystals of different lengths. Journal of Colloid and Interface Science. 630: 249-259 https://doi.org/10.1016/j.jcis.2022.10.100
53. Revol J F, Bradford H, Giasson J, et al (1992) HELICOIDAL SELF-ORDERING OF CELLULOSE MICROFIBRILS IN AQUEOUS SUSPENSION. International journal of biological macromolecules. 14: 170-172 https://doi.org/10.1016/s0141-8130(05)80008-x
54. Sacui I A, Nieuwendaal R C, Burnett D J, et al (2014) Comparison of the Properties of Cellulose Nanocrystals and Cellulose Nanofibrils Isolated from Bacteria, Tunicate, and Wood Processed Using Acid, Enzymatic, Mechanical, and Oxidative Methods. ACS applied materials & interfaces. 6: 6127-6138 https://doi.org/10.1021/am500359f
55. Segal. - L, Creely. - J J, Martin. - A E, Conrad. - C M (1959) An Empirical Method for Estimating the Degree of Crystallinity of Native Cellulose Using the X-Ray Diffractometer. Textile Research Journal. 29(1959): 786-794 https://doi.org/10.1177/004051755902901003
56. Seta F T, An X Y, Liu L Q, et al (2020) Preparation and characterization of high yield cellulose nanocrystals (CNC) derived from ball mill pretreatment and maleic acid hydrolysis. Carbohydrate polymers. 234: 10 https://doi.org/10.1016/j.carbpol.2020.115942
57. Song Q, Wang Z B, Xu D, et al (2024) Self-assembly of polysaccharide nanocrystals: from aggregation in suspensions to optical materials. Progress in Polymer Science. 148: 29 https://doi.org/10.1016/j.progpolymsci.2023.101768
58. Szymańska-Chargot M, Cybulska J, Zdunek A (2011) Sensing the Structural Differences in Cellulose from Apple and Bacterial Cell Wall Materials by Raman and FT-IR Spectroscopy. Sensors. 11: 5543-5560 https://doi.org/10.3390/s110605543
59. Velazquez G, Herrera-Gómez A, MartíN-Polo M O (2003) Identification of bound water through infrared spectroscopy in methylcellulose. Journal of Food Engineering. 59: 79-84 https://doi.org/https://doi.org/10.1016/S0260-8774(02)00428-4
60. Venkatesan R, Dhilipkumar T, Al-Sehemi A G, et al (2024) Recent advances in structural color materials based on flexible cellulose nanocrystals. Cellulose. 31: 4681-4708 https://doi.org/10.1007/s10570-024-05893-x
61. Vera R E, Suarez A, Zambrano F, et al (2023) Upcycling cotton textile waste into bio-based building blocks through an environmentally friendly and high-yield conversion process. Resources Conservation and Recycling. 189: 12

https://doi.org/10.1016/j.resconrec.2022.106715

62. Villares A, Moreau C, Bennati-Granier C, et al (2017) Lytic polysaccharide monooxygenases disrupt the cellulose fibers structure. Scientific Reports. 7: 40262 https://doi.org/10.1038/srep40262
63. Vizireanu S, Panaitescu D M, Nicolae C A, et al (2018) Cellulose defibrillation and functionalization by plasma in liquid treatment. Scientific Reports. 8: 15473 https://doi.org/10.1038/s41598-018-33687-2
64. Wang H Y, Li S Y, Wu T T, et al (2019) A Comparative Study on the Characterization of Nanofibers with Cellulose I, I/II, and II Polymorphs from Wood. Polymers. 11: 15 https://doi.org/10.3390/polym11010153
65. Wang R, Chen L, Zhu J Y, Yang R (2017) Tailored and Integrated Production of Carboxylated Cellulose Nanocrystals (CNC) with Nanofibrils (CNF) through Maleic Acid Hydrolysis. ChemNanoMat. 3: 328-335 https://doi.org/10.1002/cnma.201700015
66. Xiang Q, Lee Y Y, Pettersson P O, Torget R W (2003) Heterogeneous aspects of acid hydrolysis of α-cellulose. Applied biochemistry and biotechnology. 107: 505-514 https://doi.org/10.1385/ABAB:107:1-3:505
67. Xiaolan Z, Yingbo X, Shun Z, et al (2018) Simultaneous Structural and Quantitative Analysis of Starch from Flue-Cured Tobacco Leaves by 13C CP/MAS NMR Spectroscopy. Current Analytical Chemistry. 14: 166-173 https://doi.org/10.2174/1573411013666170731121739
68. Xing L X, Li G H, Sun Y P, et al (2023) Dual-emitting cellulose nanocrystal hybrid materials with circularly polarized luminescence for anti-counterfeiting labels. Carbohydrate polymers. 313: 11 https://doi.org/10.1016/j.carbpol.2023.120856
69. Zhang Y Y, Cheng Q Y, Chang C Y, Zhang L N (2018) Phase transition identification of cellulose nanocrystal suspensions derived from various raw materials. Journal of Applied Polymer Science. 135: 8 https://doi.org/10.1002/app.45702
70. Zhang Y Z, Zhang Y, Xu W, et al (2023) Preparation methods of cellulose nanocrystal and its application in treatment of environmental pollution: A mini-review. Colloid and Interface Science Communications. 53: 12 https://doi.org/10.1016/j.colcom.2023.100707
71. Zhou L J, Li N, Shu J, et al (2018) One-Pot Preparation of Carboxylated Cellulose Nanocrystals and Their Liquid Crystalline Behaviors. ACS Sustainable Chemistry & Engineering. 6: 12403-12410 https://doi.org/10.1021/acssuschemeng.8b02926

Figures

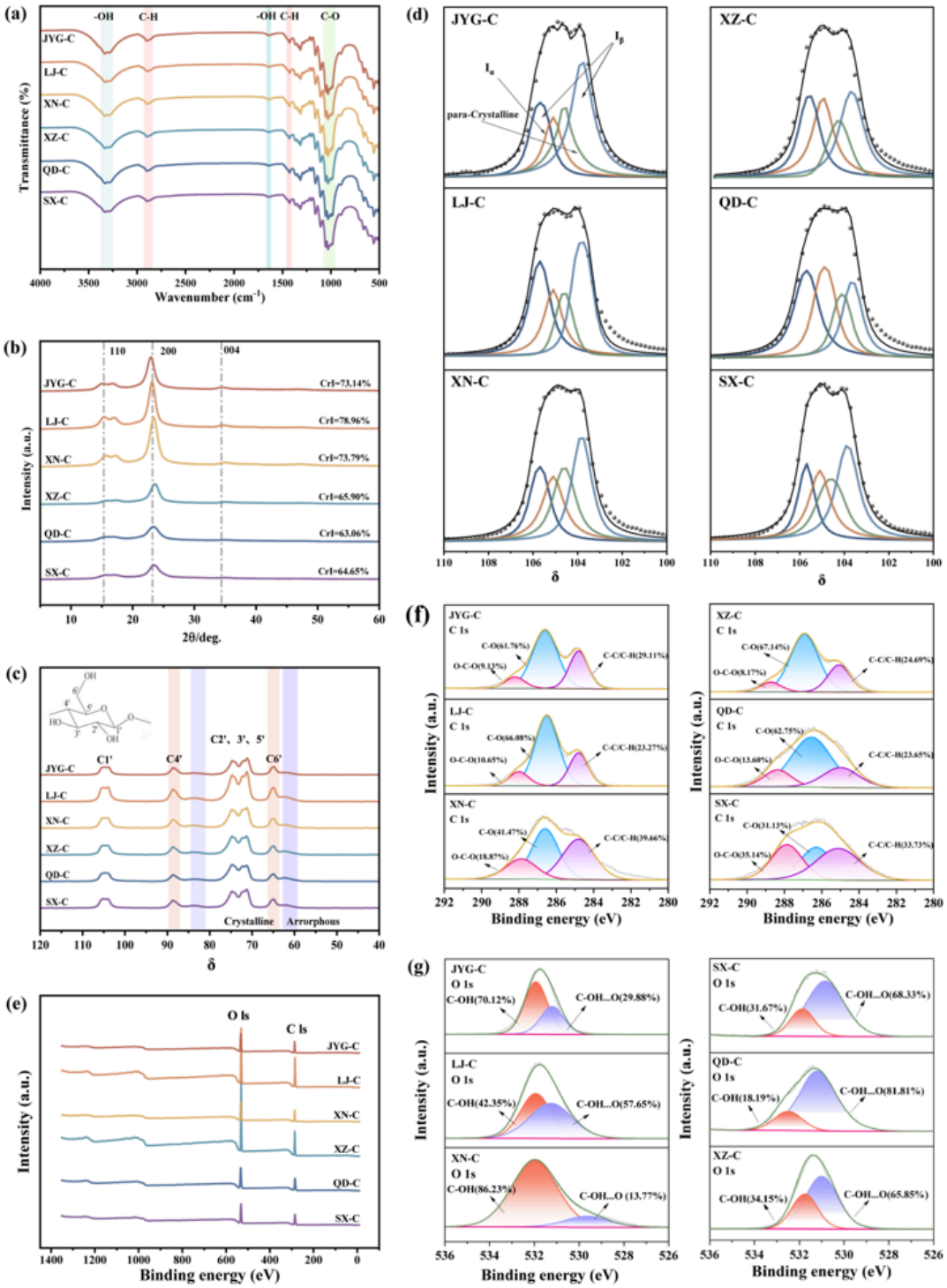


Figure 1

(a) FTIR plots of AB-C. (b) XRD plots of AB-C. (c) NMR plots of AB-C. (d) Fitting results of C1 signal peaks of NMR carbon spectra of AB-C. XPS characterization of AB-C: (e) full spectrum; (f) C 1s spectrum; (g) O 1s spectrum.

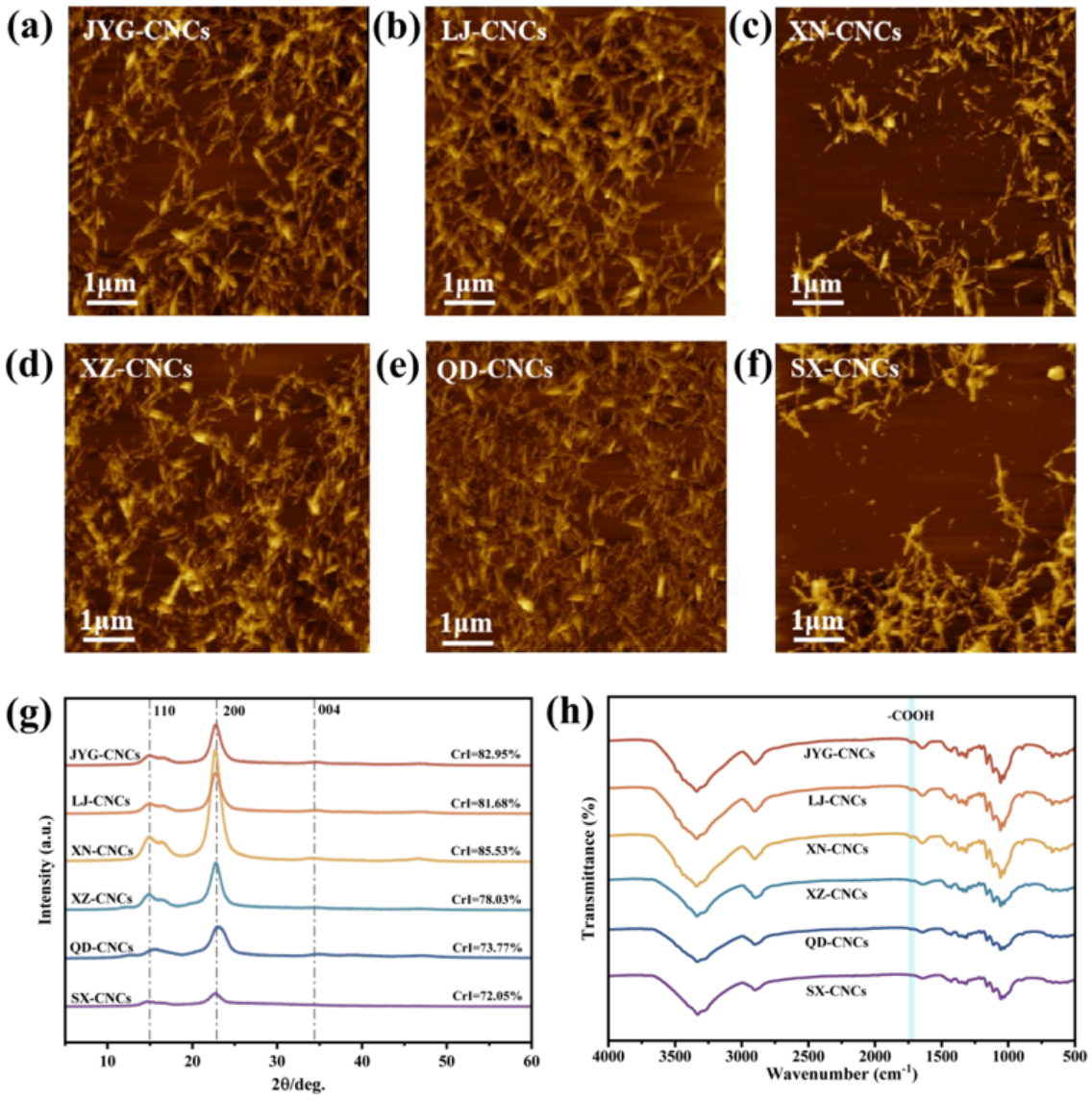


Figure 2

(a-f) AFM topographic images of C-CNCs. (g) XRD plots of C-CNCs. (h) FTIR plots of C-CNCs.

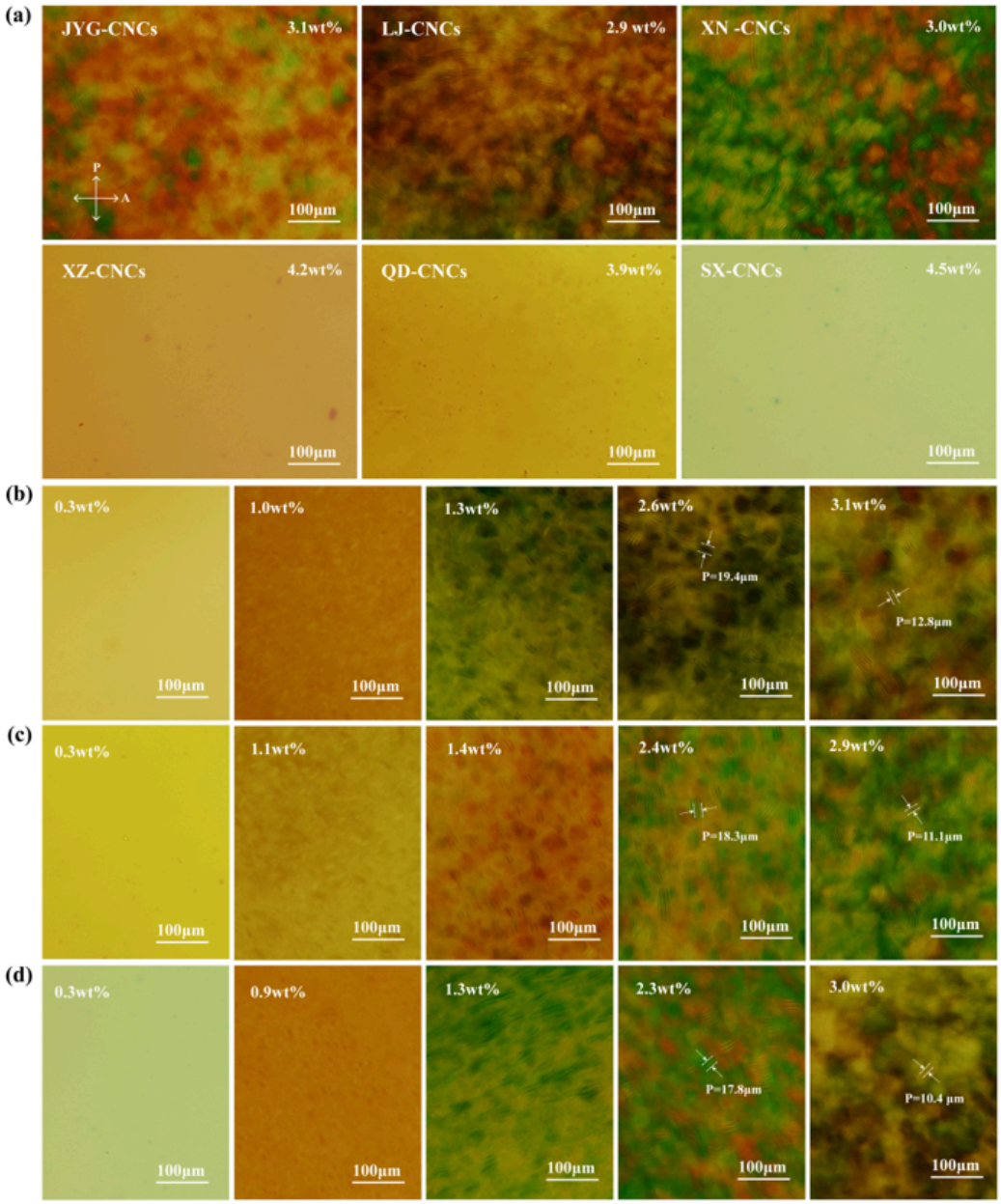


Figure 3

POM images of C-CNCs suspensions at different concentrations. (a) Overview of the six C-CNCs samples.

Detailed POM images of selected samples: (b) JYG-CNCs, (c) LJ-CNCs, and (d)XN-CNCs.

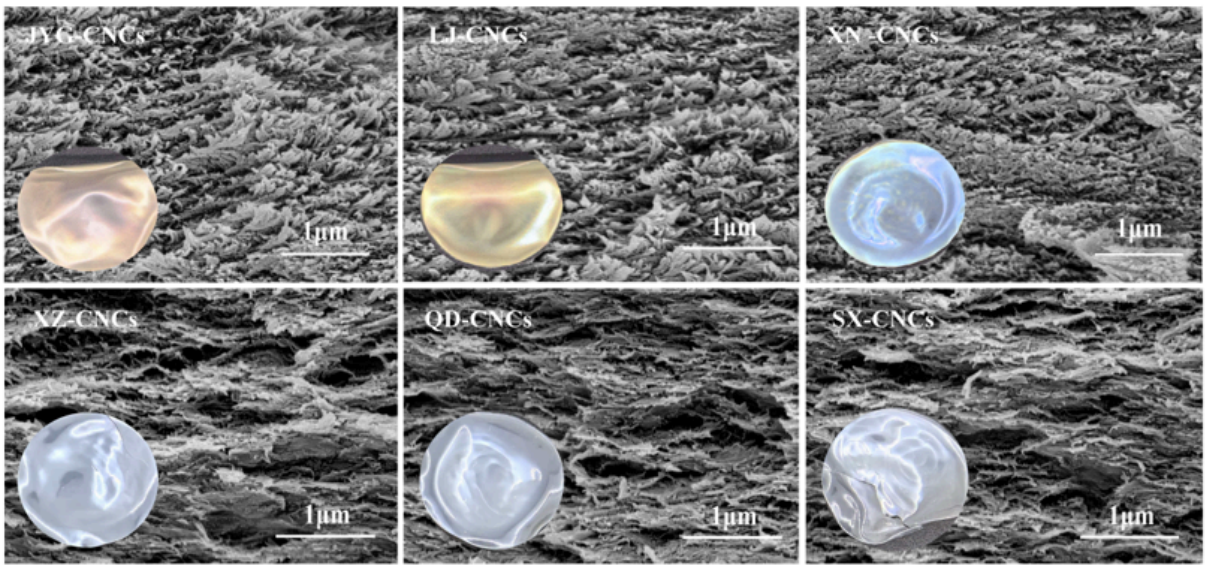


Figure 4

Digital photographs and cross-sectional SEM images of AB-CNCs films.

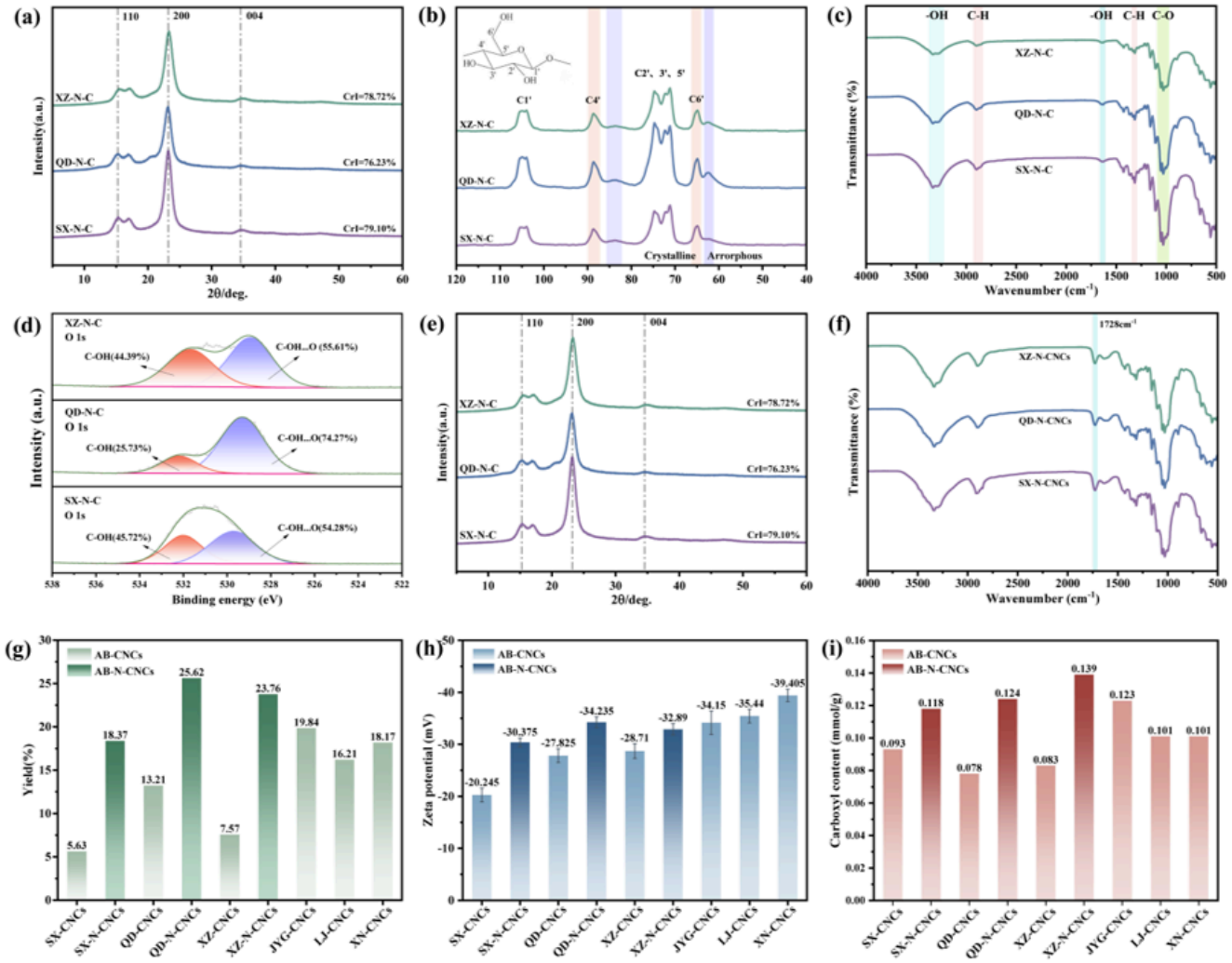


Figure 5

(a) XRD plots of AB-N-C. (b) NMR plots of AB-N-C. (c) FTIR plots of AB-N-C. (d) XPS O 1s spectrum of AB-N-C. (e) XRD plots of AB-N-CNCs. (f) FTIR plots of AB-N-CNCs. Comparative characterization of AB-CNCs and AB-N-CNCs (g) Yield; (h) Zeta potential; (i) Carboxyl content

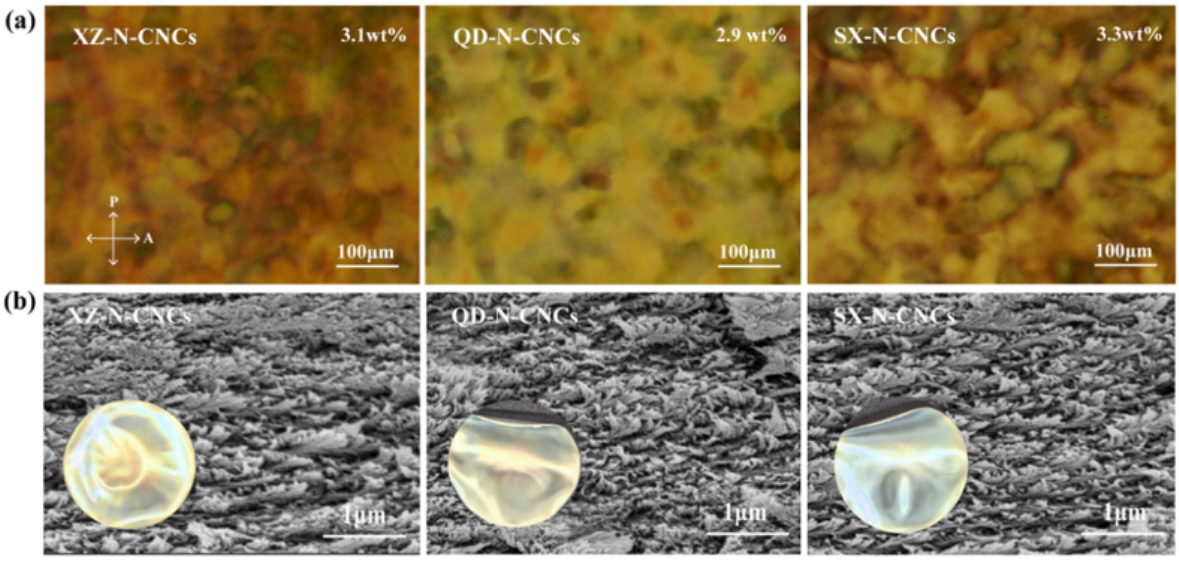


Figure 6

(a) POM images of AB-N-CNCs suspensions.

(b) Digital photographs and cross-sectional SEM images of AB-N-CNCs films.

Supplementary Files

This is a list of supplementary files associated with this preprint. Click to download.

- SupplementaryMaterial.docx
- GraphicalAbstract.docx